




Cite this: *RSC Adv.*, 2021, 11, 3174

# Probing the activity of transition metal M and heteroatom N<sub>4</sub> co-doped in vacancy fullerene (M–N<sub>4</sub>–C<sub>64</sub>, M = Fe, Co, and Ni) towards the oxygen reduction reaction by density functional theory

Siwei Yang, Chaoyu Zhao,  Ruxin Qu, Yaxuan Cheng, Huiling Liu \* and Xuri Huang\*

In this study, a novel type oxygen reduction reaction (ORR) electrocatalyst is explored using density functional theory (DFT); the catalyst consists of transition metal M and heteroatom N<sub>4</sub> co-doped in vacancy fullerene (M–N<sub>4</sub>–C<sub>64</sub>, M = Fe, Co, and Ni). Mulliken charge analysis shows that the metal center is the reaction site of ORR. PDOS analysis indicates that in M–N<sub>4</sub>–C<sub>64</sub>, the interaction between Fe–N<sub>4</sub>–C<sub>64</sub> and the adsorbate is the strongest, followed by Co–N<sub>4</sub>–C<sub>64</sub> and Ni–N<sub>4</sub>–C<sub>64</sub>. This is consistent with the calculated adsorption energies. By analyzing and comparing the adsorption energies of ORR intermediates and activation energies and reaction energies of all elemental reactions in M–N<sub>4</sub>–C<sub>64</sub> (M = Fe, Co, and Ni), two favorable ORR electrocatalysts, Fe–N<sub>4</sub>–C<sub>64</sub> and Co–N<sub>4</sub>–C<sub>64</sub>, are selected. Both exhibited conduction through the more efficient 4e<sup>−</sup> reduction pathway. Moreover, PES diagrams indicate that the whole reaction energy variation in the favorable ORR pathways of Fe–N<sub>4</sub>–C<sub>64</sub> and Co–N<sub>4</sub>–C<sub>64</sub> is degressive, which is conducive to positive-going reactions. This study offers worthwhile information for the improvement of cathode materials for fuel cells.

Received 11th October 2020  
Accepted 19th December 2020

DOI: 10.1039/d0ra08652e

rsc.li/rsc-advances

## 1. Introduction

With the expansion of industrialization and urbanization, environmental pollution and energy consumption are being increasingly aggravated. Fuel cells (FCs) have become the most promising power generation technology, with the characteristics of sustainable, pollution-free and wide-ranging fuel sources.<sup>1–4</sup> The oxygen reduction reaction (ORR) is carried out in the cathode through 2e<sup>−</sup> and 4e<sup>−</sup> pathways.<sup>5,6</sup> The 4e<sup>−</sup> pathway directly reduces O<sub>2</sub> to H<sub>2</sub>O and has high energy conversion efficiency; hence, it is the preferred pathway for FCs.<sup>7,8</sup> However, the 2e<sup>−</sup> pathway (the less efficient pathway involving the formation of H<sub>2</sub>O<sub>2</sub> as an intermediate) and slow kinetics on the cathode hinder the power generation efficiency of FCs.<sup>9–11</sup> In addition, Pt-based catalysts, which are considered to be highly efficient,<sup>12,13</sup> have limited commercial applications in FCs due to their high cost.<sup>14,15</sup> Therefore, it is urgent to exploit high-performance and inexpensive ORR electrocatalysts to substitute the expensive Pt-based catalysts on the market.

Because single-atom catalysts (SACs) have different activity, selectivity and stability from traditional nanocatalysts,<sup>16,17</sup> they

are proposed to exhibit remarkable behavior in various energy transformation reactions, such as HER,<sup>18,19</sup> CO<sub>2</sub>RR<sup>20,21</sup> and ORR.<sup>22,23</sup> Moreover, the realization of single-atom dispersion of SACs usually requires a suitable substrate and dopant.<sup>24</sup> Fullerenes are cage structures in which carbon atoms form a conjugated system through sp<sup>2</sup> hybridization.<sup>25</sup> As non-metallic materials with a wide range of sources, fullerenes have demonstrated excellent performance including biological applications,<sup>26</sup> energy storage,<sup>27</sup> thermoelectric materials,<sup>28</sup> and optoelectronic devices.<sup>29</sup> In addition, as a result of the curvature and pentagon defects of fullerenes,<sup>30,31</sup> they can be used as promising candidates for electrocatalytic reactions. Vinu *et al.* investigated a polymeric mesoporous fullerene C<sub>60</sub> material prepared at 130 °C (MFC<sub>60</sub>-130), which showed effective ORR behavior benefiting from its specific surface area of 680 m<sup>2</sup> g<sup>−1</sup> and steady and conductive C<sub>60</sub> reticulation.<sup>32</sup> Subsequently, Vinu *et al.* continued to report mesoporous fullerene C<sub>70</sub> materials, which were endowed with good mesoporous framework, excellent conductivity and connectivity; further, materials exhibited good ORR performance.<sup>33</sup> However, it is necessary to improve their electrocatalytic properties for practical applications.

Heteroatom doping is an effectual way to regulate the electronic and conductive properties of fullerenes and enhance their electrocatalytic behavior.<sup>34,35</sup> Chen *et al.* discovered that

Laboratory of Theoretical and Computational Chemistry, Institute of Theoretical Chemistry, Jilin University, Liutiao Road 2, Changchun 130023, China. E-mail: huiling@jlu.edu.cn; huangxr@jlu.edu.cn



nitrogen-doped fullerenes showed higher ORR properties than pure fullerenes.<sup>36</sup> Wang *et al.* also reported that nitrogen-doped C<sub>60</sub> cages (C<sub>59</sub>N) exhibited superior ORR electrocatalytic activity to other heteroatom-doped C<sub>60</sub> cages,<sup>37</sup> which was further experimentally proved by Gao *et al.*<sup>35</sup>

Furthermore, to facilitate the embedding of metal atoms, introducing vacancies in the substrate can change the coordination environment and electronic structure around the vacancies; thus, under-coordinated sites can act as bait and vacancies can act as traps to trap metal atoms.<sup>38,39</sup> The co-doping of transition metal atoms and heteroatoms on vacant carbon materials has been widely studied both experimentally and theoretically. Fe-porphyrin-like carbon nanotubes synthesized by Lee *et al.* showed excellent oxygen reduction activity due to the characteristics of the Fe-N<sub>4</sub> structure.<sup>40</sup> Fei *et al.* found that the composite material obtained by embedding individual Ni atoms into the double vacancies of an N-doped graphene lattice displayed higher oxygen evolution reaction (OER) activity and stability.<sup>41</sup> Chen *et al.* embedded individual iron atoms into N-pore carbon through the thermolysis approach of cage-encapsulated precursors, and the composite exhibited remarkable ORR properties and satisfactory methanol tolerance.<sup>42</sup> Recently, Wang *et al.* reported synthesized Fe-anchored graphite carbonitride, which was used in CO<sub>2</sub>RR to improve the selectivity of CO and realize the high-efficiency transformation of CO<sub>2</sub> due to the Fe-N<sub>4</sub> sites in the composite.<sup>43</sup> Theoretically, many studies have illuminated that metal-N<sub>4</sub>-vacancy carbon materials have attractive performance as cathode materials for FCs.<sup>44–47</sup> Significantly, Brindaban Modak *et al.* found that transition metal-modified porous fullerene C<sub>24</sub>N<sub>24</sub> can serve as an oxygen reduction electrocatalyst and carry out a more effectual 4e<sup>−</sup> reduction mechanism.<sup>48</sup> These reports led us to wonder whether transition metal and heteroatom N could be co-doped in vacancy fullerenes as effective electrocatalysts for ORR. However, related reports are rare. Therefore, we systematically studied all possible intermediate steps involved in the ORR process of co-doping transition metal M and heteroatom N<sub>4</sub> in vacancy fullerene (M-N<sub>4</sub>-C<sub>64</sub>, M = Fe, Co, and Ni). The promising ORR electrocatalysts were selected and the corresponding favorable ORR pathways were determined. This work offers worthwhile information for the improvement of cathode materials for FCs.

## 2. Computational methods

All calculations were carried out using the spin-polarized DFT implemented in Materials Studio DMol<sup>3</sup> code.<sup>36,49</sup> The generalized gradient approximation of the Perdew–Burke–Ernzerhof functional (GGA + PBE),<sup>48,50</sup> together with all electrons and the double numerical basis set (DNP), was adopted throughout all calculations. To improve computational performance, the self-consistent field (SCF) was converged to 10<sup>−6</sup> Ha and the smearing was set to 0.005 Ha. The convergence tolerance was 2 × 10<sup>−5</sup> Ha for the energy change, 0.004 Ha Å<sup>−1</sup> for the max force and 0.005 Å for the max displacement. The Grimme method for DFT-D correction was used to describe the van der Waals

interactions. The energy difference between the transition state and the reactant was the activation barrier (*E*<sub>act</sub>).

The formation energy (*E*<sub>f</sub>) of M-N<sub>4</sub> co-doped in vacancy fullerene was calculated as follows:

$$E_f = E_{M-N_4-C_{64}} + 6\mu_C - (E_{\text{fullerene}} + 4\mu_N + E_M)$$

where *E*<sub>M-N<sub>4</sub>-C<sub>64</sub></sub> and *E*<sub>fullerene</sub> are the energies of the optimized M-N<sub>4</sub>-C<sub>64</sub> and perfect fullerene C<sub>70</sub>, correspondingly. *μ*<sub>C</sub> and *μ*<sub>N</sub> are the chemical potentials of carbon and nitrogen atoms, which were obtained by the total energy per C atom in perfect fullerene C<sub>70</sub> and one half of an N<sub>2</sub> gas molecule, correspondingly. *E*<sub>M</sub> is the energy of the individual metal atom.

The adsorption energy (*E*<sub>ads</sub>) was calculated as follows:

$$E_{\text{ads}} = E_{\text{adsorbate}@M-N_4-C_{64}} - E_{M-N_4-C_{64}} - E_{\text{adsorbate}}$$

where *E*<sub>adsorbate@M-N<sub>4</sub>-C<sub>64</sub></sub>, *E*<sub>M-N<sub>4</sub>-C<sub>64</sub></sub> and *E*<sub>adsorbate</sub> refer to the energies of M-N<sub>4</sub>-C<sub>64</sub> (M = Fe, Co, and Ni) with the adsorbate, individual M-N<sub>4</sub>-C<sub>64</sub> and the individual adsorbate, correspondingly.

## 3. Results and discussion

### 3.1 Configuration and properties of M-N<sub>4</sub>-C<sub>64</sub>

To embed M-N<sub>4</sub> in fullerene, as Fig. 1a shows, the no. 1 and 2 carbon atoms in the optimized fullerene C<sub>70</sub> were removed. Then, four nitrogen atoms were utilized to substitute the no. 3, 4, 5 and 6 carbon atoms, which had insufficient coordination. Finally, the metal atom was incorporated in the center of the vacancy. We calculated the different multiplicities of M-N<sub>4</sub>-C<sub>64</sub> (M = Fe, Co, and Ni) to obtain the most stable energies. The results show that the most stable states for Fe-N<sub>4</sub>-C<sub>64</sub>, Co-N<sub>4</sub>-

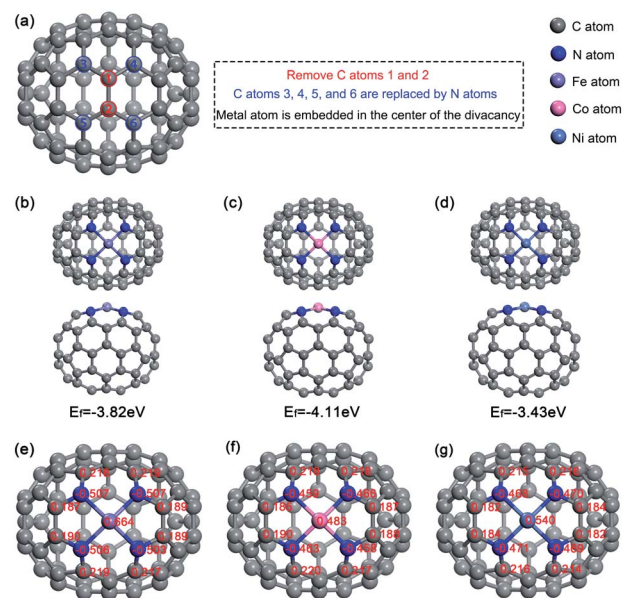


Fig. 1 The optimized configurations of (a) C<sub>70</sub>, (b) Fe-N<sub>4</sub>-C<sub>64</sub>, (c) Co-N<sub>4</sub>-C<sub>64</sub> and (d) Ni-N<sub>4</sub>-C<sub>64</sub>. Charge distributions on (e) Fe-N<sub>4</sub>-C<sub>64</sub>, (f) Co-N<sub>4</sub>-C<sub>64</sub> and (g) Ni-N<sub>4</sub>-C<sub>64</sub>.



$C_{64}$ , and  $Ni-N_4-C_{64}$  are triplet, doublet, and singlet, correspondingly. The oxygen molecule is a triplet in our research system. The stable configurations of  $Fe-N_4-C_{64}$ ,  $Co-N_4-C_{64}$  and  $Ni-N_4-C_{64}$  were optimized (see Fig. 1b–d), and the formation energies ( $E_f$ ) of the three configurations were calculated as  $-3.82$ ,  $-4.11$ , and  $-3.43$  eV, correspondingly. This finding demonstrates that  $Fe-N_4-C_{64}$ ,  $Co-N_4-C_{64}$  and  $Ni-N_4-C_{64}$  are thermodynamically stable. In addition, as can be seen from the Mulliken charges in Fig. 1e–g, nitrogen atoms in  $M-N_4-C_{64}$  ( $M = Fe, Co$ , and  $Ni$ ) show negative charge density, while the adjacent carbon atoms show positive charge density. This is caused by the fact that the electronegativity of N atoms is greater than that of C atoms. This porphyrin-like structure can stably fix  $M-N_4$  embedded on  $C_{64}$ . The Mulliken charges of the Fe, Co and Ni atoms were calculated as  $0.664$ ,  $0.483$  and  $0.540|e|$ , correspondingly. Because a positively charged site is more advantageous for  $O_2$  adsorption, the metal center was chosen as the reaction site for ORR. On the other hand, it was found that in the  $Fe-N_4-C_{64}$  system, the electron transfer from the metal center to  $N_4-C_{64}$  is the largest.

### 3.2 Electronic structure of $M-N_4-C_{64}$

The calculated DOS (see Fig. 2a) display that the band gaps of  $Fe-N_4-C_{64}$ ,  $Co-N_4-C_{64}$  and  $Ni-N_4-C_{64}$  are all zero, which reveals that they have the potential to be ORR electrocatalysts due to their excellent electrical conductivity.

The calculated PDOS (see Fig. 2b–d) display that the C-2p and N-2p orbitals in  $M-N_4-C_{64}$  ( $M = Fe, Co$ , and  $Ni$ ) exhibit strong resonance regions below the Fermi level, which indicates that the interaction between C and N is very strong. Meanwhile, the PDOS display that in  $M-N_4-C_{64}$ , the Co-3d orbital contribution is the most average below the Fermi level, followed by Fe-3d and finally Ni-3d, which is consistent with stability of the

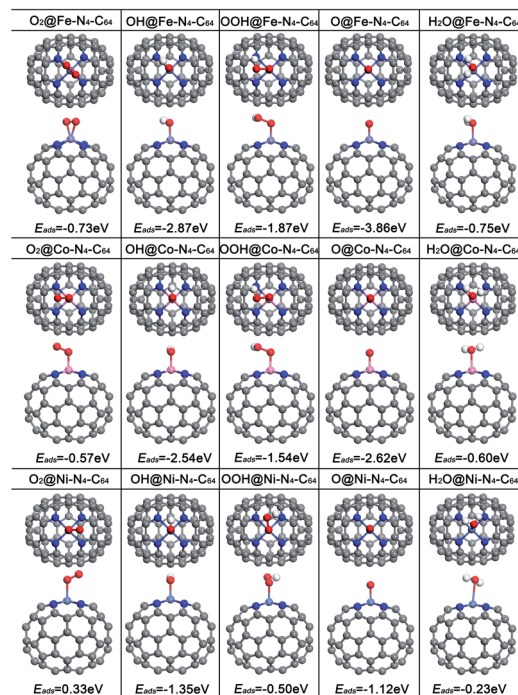


Fig. 3 The optimized configurations of the adsorption of  $O_2$ , OH, OOH, O and  $H_2O$  on  $Fe-N_4-C_{64}$ ,  $Co-N_4-C_{64}$  and  $Ni-N_4-C_{64}$ .

calculated  $E_f$  for  $M-N_4-C_{64}$ . In addition, the calculated d-band centers in the range of  $-8.0$  eV– $4$  eV are  $-1.24$  eV for  $Fe-N_4-C_{64}$ ,  $-1.33$  eV for  $Co-N_4-C_{64}$  and  $-1.61$  eV for  $Ni-N_4-C_{64}$ , which demonstrates that the interaction between  $Fe-N_4-C_{64}$  and the adsorbate is the strongest among the three, followed by  $Co-N_4-C_{64}$  and finally  $Ni-N_4-C_{64}$ . This is attributable to the fact that the upward shift of the d-band center to the Fermi level will arouse the upward shift of the antibonding orbitals; thus, they are

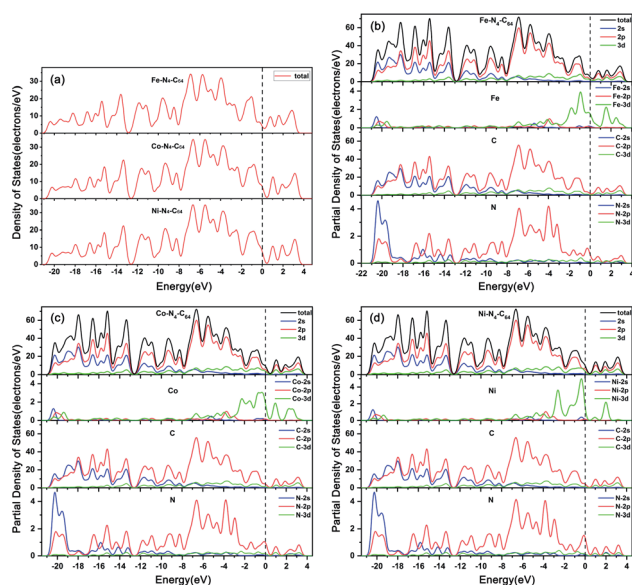


Fig. 2 (a) The densities of states for  $Fe-N_4-C_{64}$ ,  $Co-N_4-C_{64}$  and  $Ni-N_4-C_{64}$ . The partial densities of states for (b)  $Fe-N_4-C_{64}$ , (c)  $Co-N_4-C_{64}$  and (d)  $Ni-N_4-C_{64}$ .

Table 1 Activation barriers ( $E_{act}$ ), reaction energies ( $\Delta E$ ) and virtual frequencies ( $\nu_{freq}$ ) of the basic reaction steps for the ORR on  $M-N_4-C_{64}$  ( $M = Fe, Co$ , and  $Ni$ )

Catalysts	Reaction steps	$E_{act}$ (eV)	$\Delta E$ (eV)	$\nu_{freq}$ ( $cm^{-1}$ )
$Fe-N_4-C_{64}$	$*O_2 \rightarrow *O + *O$	2.25	0.40	$i439$
	$*O_2 + *H \rightarrow *OOH$	0.06	$-0.97$	$i1514$
	$*OOH + *H \rightarrow *H_2O_2$	2.77	$-0.31$	$i1026$
	$*OOH + *H \rightarrow *O + *H_2O$	0.32	$-1.21$	$i1355$
	$*O + *H \rightarrow *OH$	0.34	$-1.35$	$i1298$
	$*OH + *H \rightarrow *H_2O$	0.47	$-0.60$	$i1426$
$Co-N_4-C_{64}$	$*O_2 \rightarrow *O + *O$	2.93	1.46	$i561$
	$*O_2 + *H \rightarrow *OOH$	0.13	$-0.69$	$i981$
	$*OOH + *H \rightarrow *H_2O_2$	0.80	$-0.46$	$i1469$
	$*H_2O_2 \rightarrow *O + *H_2O$	0.33	$-0.23$	$i627$
	$*OOH + *H \rightarrow *O + *H_2O$	0.78	$-0.41$	$i768$
	$*O + *H \rightarrow *OH$	0.04	$-2.10$	$i918$
$Ni-N_4-C_{64}$	$*OH + *H \rightarrow *H_2O$	0.22	$-0.86$	$i1467$
	$*O_2 + *H \rightarrow *OOH$	0.08	$-0.36$	$i1102$
	$*OOH + *H \rightarrow *O + *H_2O$	0.68	0.21	$i454$
	$*O + *H \rightarrow *OH$	3.25	$-2.43$	$i468$
	$*OH + *H \rightarrow *H_2O$	2.97	$-1.93$	$i767$





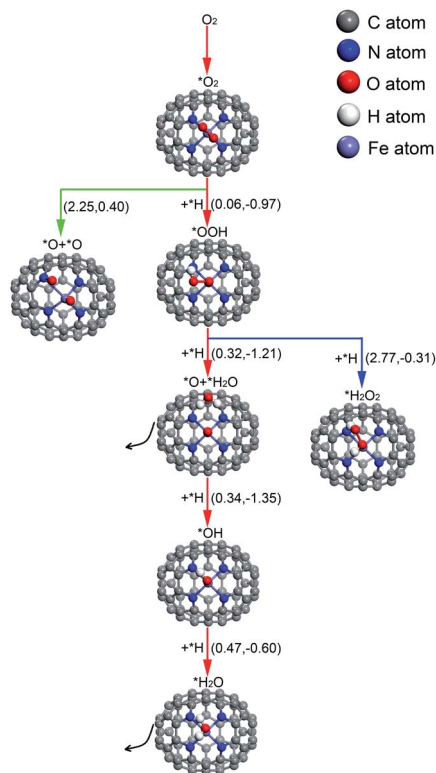


Fig. 4 The conceivable ORR pathways on Fe-N<sub>4</sub>-C<sub>64</sub>. The value on the left in parentheses is the activation energy and the value on the right is the reaction energy (in eV). \* indicates adsorbed species.

harder to fill, and in turn, the interaction between the catalyst and adsorbates is stronger.

### 3.3 The adsorption of ORR species on M-N<sub>4</sub>-C<sub>64</sub>

The adsorption of ORR species plays a formative role in the study of the ORR mechanism and electrocatalytic activity. For comparison, Fig. 3 exhibits the optimized adsorption configurations of the ORR species (O<sub>2</sub>, OH, OOH, O and H<sub>2</sub>O) on M-N<sub>4</sub>-C<sub>64</sub> (M = Fe, Co, and Ni), and the corresponding adsorption energies ( $E_{\text{ads}}$ ) were calculated. The results manifest that  $E_{\text{ads}}$  weakens in this sequence: Fe-N<sub>4</sub>-C<sub>64</sub> > Co-N<sub>4</sub>-C<sub>64</sub> > Ni-N<sub>4</sub>-C<sub>64</sub>, which is in line with the results of the PDOS analysis. The electrocatalytic capability of the catalyst can be exhibited visually by the chemisorption of O<sub>2</sub> molecule on the substrate as the preliminary stage of ORR. The O<sub>2</sub> molecule is stably adsorbed on the Fe center of Fe-N<sub>4</sub>-C<sub>64</sub> by side-on configuration, and the  $E_{\text{ads}}$  was calculated as  $-0.73$  eV. After adsorption,  $d_{\text{O-O}}$  is  $1.345$  Å ( $d_{\text{A-B}}$  represents the distance between A and B), which is increased compared with that of the individual O<sub>2</sub> molecule ( $1.225$  Å). The O<sub>2</sub> is stably adsorbed on the Co center of Co-N<sub>4</sub>-C<sub>64</sub> by end-on configuration, and the  $E_{\text{ads}}$  was calculated as  $-0.57$  eV. After adsorption,  $d_{\text{O-O}}$  is  $1.270$  Å, which is slightly larger than that of the individual O<sub>2</sub> molecule ( $1.225$  Å). However, in the Ni-N<sub>4</sub>-C<sub>64</sub> system, the calculated  $E_{\text{ads}}$  of the O<sub>2</sub> is  $0.33$  eV, and the positive value of  $E_{\text{ads}}$  indicates that it is unbound relative to the separated O<sub>2</sub>. This indicates that the ORR behavior of Ni-N<sub>4</sub>-C<sub>64</sub> is disadvantageous. Atomic O is adsorbed on Fe-N<sub>4</sub>-C<sub>64</sub> and Co-N<sub>4</sub>-C<sub>64</sub> with the strongest  $E_{\text{ads}}$

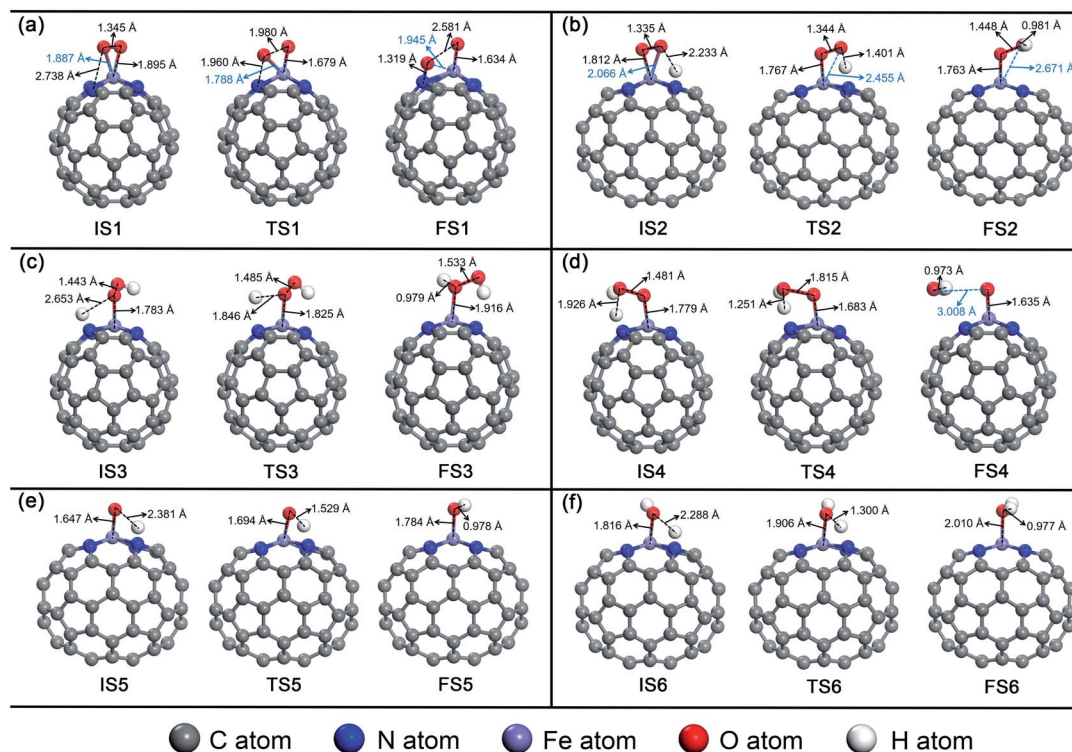


Fig. 5 The detailed process of the ORR on Fe-N<sub>4</sub>-C<sub>64</sub>. (a)  $\text{O}_2 \rightarrow \text{*O} + \text{*O}$ , (b)  $\text{O}_2 + \text{*H} \rightarrow \text{*OOH}$ , (c)  $\text{*OOH} + \text{*H} \rightarrow \text{*H}_2\text{O}_2$ , (d)  $\text{*OOH} + \text{*H} \rightarrow \text{*O} + \text{*H}_2\text{O}$ , (e)  $\text{*O} + \text{*H} \rightarrow \text{*OH}$ , and (f)  $\text{*OH} + \text{*H} \rightarrow \text{*H}_2\text{O}$ .



values of  $-3.86$  and  $-2.62$  eV, correspondingly. The  $E_{\text{ads}}(\text{OH})$  for  $\text{M-N}_4\text{-C}_{64}$  ( $\text{M} = \text{Fe}, \text{Co}, \text{and Ni}$ ) is larger than that of  $E_{\text{ads}}(-\text{OOH})$ . Furthermore, for the ORR product  $\text{H}_2\text{O}$ , the  $E_{\text{ads}}$  is  $-0.75$  eV for  $\text{Fe-N}_4\text{-C}_{64}$ ,  $-0.60$  eV for  $\text{Co-N}_4\text{-C}_{64}$  and  $-0.23$  eV for  $\text{Ni-N}_4\text{-C}_{64}$ . These weak  $E_{\text{ads}}$  values are close to the solvation energy ( $\sim -0.40$  eV) of massive  $\text{H}_2\text{O}$ .<sup>45,51</sup> Therefore, once  $\text{H}_2\text{O}$  is formed, it can be effortlessly separated from  $\text{M-N}_4\text{-C}_{64}$ .

### 3.4 ORR mechanisms on $\text{M-N}_4\text{-C}_{64}$

The ORR mechanisms on  $\text{M-N}_4\text{-C}_{64}$  ( $\text{M} = \text{Fe}, \text{Co}, \text{and Ni}$ ) are complicated. To prove that the three catalysts can serve as effective ORR electrocatalysts, we will systematically study the ORR mechanisms of the three systems in the following sections. The activation barriers ( $E_{\text{act}}$ ), reaction energies ( $\Delta E$ ) and virtual frequencies ( $V_{\text{freq}}$ ) of all the ORR basic reaction steps involved in  $\text{M-N}_4\text{-C}_{64}$  ( $\text{M} = \text{Fe}, \text{Co}, \text{and Ni}$ ) are listed in Table 1.

**3.4.1 ORR mechanisms on  $\text{Fe-N}_4\text{-C}_{64}$ .** The ORR mechanisms on  $\text{Fe-N}_4\text{-C}_{64}$  were studied, and all conceivable pathways are placed in Fig. 4, where the red line pathway represents the optimal summarized ORR mechanism for  $\text{Fe-N}_4\text{-C}_{64}$ . The details of the ORR on  $\text{Fe-N}_4\text{-C}_{64}$  will be discussed next.

For  $\text{O}_2$  chemisorbed on  $\text{Fe-N}_4\text{-C}_{64}$ , there are two conceivable pathways: dissociation ( $^*\text{O}_2 \rightarrow ^*\text{O} + ^*\text{O}$ ) and hydrogenation ( $^*\text{O}_2 + ^*\text{H} \rightarrow ^*\text{OOH}$ ) (\* indicates adsorbed species). For  $^*\text{O}_2 \rightarrow ^*\text{O} + ^*\text{O}$ , this reaction requires an endothermic reaction energy of  $0.40$  eV and is accompanied by a high activation barrier ( $E_{\text{act}}$ ) of  $2.25$  eV. This indicates that the stage of  $^*\text{O}_2 \rightarrow ^*\text{O} + ^*\text{O}$  on  $\text{Fe-N}_4\text{-C}_{64}$  is disadvantageous in thermodynamics and kinetics. The dissociation details are presented in Fig. 5a. Conversely, the hydrogenation of  $^*\text{O}_2$  to  $^*\text{OOH}$  is more feasible because for  $^*\text{O}_2 + ^*\text{H} \rightarrow ^*\text{OOH}$ , this reaction has an exothermic reaction energy of  $0.97$  eV. Moreover, this process is accompanied by an extremely low  $E_{\text{act}}$  of  $0.06$  eV, which is obviously lower than the  $E_{\text{ads}}$  of  $^*\text{O}_2$  ( $-0.73$  eV) on  $\text{Fe-N}_4\text{-C}_{64}$ . The virtual frequency ( $V_{\text{freq}}$ ) of  $1514\text{ cm}^{-1}$  in the transition state TS2 exactly shows the formation of the intermediate  $^*\text{OOH}$ . The hydrogenation details (see Fig. 5b) indicate that  $d_{\text{O-H}}$  decreases from  $2.233\text{ \AA}$  in IS2 to  $1.401\text{ \AA}$  in TS2 and to  $0.981\text{ \AA}$  in FS2. Meanwhile, the distance between the atomic O which is attacked by the atomic H and the Fe atom extends from  $2.066\text{ \AA}$  in IS2 to  $2.455\text{ \AA}$  in TS2 and to  $2.671\text{ \AA}$  in FS2, and the  $^*\text{OOH}$  intermediate in FS2 is adsorbed on the Fe site by end-on configuration. Furthermore,  $d_{\text{O-O}}$  extends from  $1.335\text{ \AA}$  in IS2 to  $1.448\text{ \AA}$  in FS2, which indicates that the interaction between the two O atoms is weakened and subsequent reactions will occur.

For the formed  $^*\text{OOH}$ , there are two conceivable hydrogenation pathways: the  $^*\text{H}$  attacks the O atom that bonds to Fe to afford  $^*\text{H}_2\text{O}_2$  ( $^*\text{OOH} + ^*\text{H} \rightarrow ^*\text{H}_2\text{O}_2$ ), or  $^*\text{H}$  attacks the hydroxyl oxygen in  $^*\text{OOH}$  to afford  $^*\text{O}$  and  $^*\text{H}_2\text{O}$  ( $^*\text{OOH} + ^*\text{H} \rightarrow ^*\text{O} + ^*\text{H}_2\text{O}$ ). For  $^*\text{OOH} + ^*\text{H} \rightarrow ^*\text{H}_2\text{O}_2$ , this reaction is accompanied by an insurmountable  $E_{\text{act}}$  of  $2.77$  eV, which manifests that the  $2e^-$  pathway to generate  $^*\text{H}_2\text{O}_2$  on  $\text{Fe-N}_4\text{-C}_{64}$  is kinetically infeasible. This hydrogenation details are described in Fig. 5c. Conversely, the reaction  $^*\text{OOH} + ^*\text{H} \rightarrow ^*\text{O} + ^*\text{H}_2\text{O}$  releases  $1.21$  eV of energy with a low  $E_{\text{act}}$  of  $0.32$  eV, which is more feasible under the support of thermodynamics and kinetics.

Moreover, the energy required for this stage is notably lower than the  $E_{\text{ads}}$  of  $^*\text{OOH}$  ( $-1.87$  eV) on  $\text{Fe-N}_4\text{-C}_{64}$ . The  $V_{\text{freq}}$  of  $1355\text{ cm}^{-1}$  in TS4 exactly exhibits the formation of  $^*\text{H}_2\text{O}$ , and the formed  $^*\text{H}_2\text{O}$  can be effortlessly detached from the  $\text{Fe-N}_4\text{-C}_{64}$  surface, which only requires a very low energy of  $0.27$  eV. The hydrogenation details (see Fig. 5d) indicate that  $d_{\text{Fe-O}}$  shortens from  $1.779\text{ \AA}$  in IS4 to  $1.635\text{ \AA}$  in FS4 and  $d_{\text{O-O}}$  increases from  $1.481\text{ \AA}$  in IS4 to  $3.008\text{ \AA}$  in FS4. This indicates that the interaction between Fe-O is strengthened and the O-O bond is broken.

Finally, the atomic O remaining on Fe experiences continuous hydrogenation to afford the second  $^*\text{H}_2\text{O}$ :  $^*\text{O} + ^*\text{H} \rightarrow ^*\text{OH}$  and  $^*\text{OH} + ^*\text{H} \rightarrow ^*\text{H}_2\text{O}$ . The former reaction has a large exothermic reaction energy of  $1.35$  eV. Moreover, this process is accompanied by a low  $E_{\text{act}}$  of  $0.34$  eV, which is significantly lower than the  $E_{\text{ads}}$  of  $^*\text{O}$  ( $-3.86$  eV) on  $\text{Fe-N}_4\text{-C}_{64}$ . The hydrogenation details (see Fig. 5e) indicate that  $d_{\text{O-H}}$  diminishes from  $2.381\text{ \AA}$  in IS5 to  $0.978\text{ \AA}$  in FS5. Moreover, in TS5, the Fe-O bond is tilted to promote the formation of  $^*\text{OH}$ . The  $d_{\text{Fe-O}}$  length increases from  $1.647\text{ \AA}$  in IS5 to  $1.784\text{ \AA}$  in FS5, which manifests that the interaction between Fe-O is weakened with the formation of  $^*\text{OH}$ . Then, the  $^*\text{OH}$  remaining on Fe experiences the succeeding hydrogenation:  $^*\text{OH} + ^*\text{H} \rightarrow ^*\text{H}_2\text{O}$ . This stage has an exothermic reaction energy of  $0.60$  eV. Moreover,

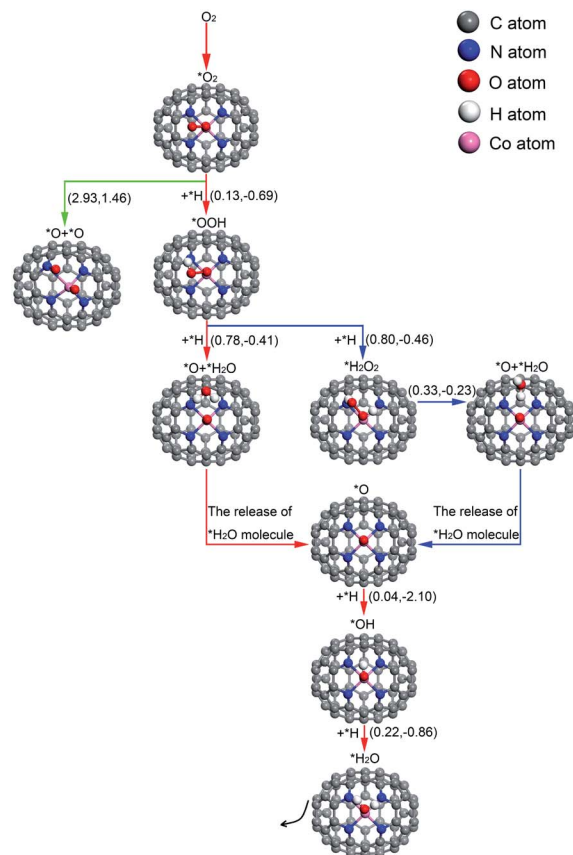


Fig. 6 The conceivable ORR pathways on  $\text{Co-N}_4\text{-C}_{64}$ . The value on the left in parentheses is the activation energy and the value on the right is the reaction energy (in eV). \* means adsorbed species.

this process is accompanied by a low  $E_{\text{act}}$  of 0.47 eV, which is significantly lower than the  $E_{\text{ads}}$  of  $^*\text{OH}$  (−2.87 eV) on  $\text{Fe-N}_4\text{-C}_{64}$ . The hydrogenation details (see Fig. 5f) indicate that the  $d_{\text{Fe-O}}$  lengthens from 1.816 Å in IS6 to 2.010 Å in FS6, which indicates that the interaction between Fe–O is weakened, and the formed  $^*\text{H}_2\text{O}$  can be easily detached from the  $\text{Fe-N}_4\text{-C}_{64}$  surface due to its low  $E_{\text{ads}}$  of −0.75 eV.  $V_{\text{freq}}$  is  $i1298\text{ cm}^{-1}$  for TS5 and  $i1426\text{ cm}^{-1}$  for TS6, respectively. This describes the formation of  $^*\text{OH}$  and the second  $^*\text{H}_2\text{O}$ .

**3.4.2 ORR mechanisms on  $\text{Co-N}_4\text{-C}_{64}$ .** The ORR mechanisms on  $\text{Co-N}_4\text{-C}_{64}$  were studied, and all conceivable pathways are shown in Fig. 6, where the red and blue lines represent the two pathways that facilitate the ORR on  $\text{Co-N}_4\text{-C}_{64}$ . The details of the ORR on  $\text{Co-N}_4\text{-C}_{64}$  will be discussed next.

For  $\text{O}_2$  chemisorbed on  $\text{Co-N}_4\text{-C}_{64}$ , there are two conceivable pathways: dissociation ( $^*\text{O}_2 \rightarrow ^*\text{O} + ^*\text{O}$ ) and hydrogenation ( $^*\text{O}_2 + ^*\text{H} \rightarrow ^*\text{OOH}$ ). For  $^*\text{O}_2 \rightarrow ^*\text{O} + ^*\text{O}$ , this reaction requires a large endothermic reaction energy of 1.46 eV and is accompanied by an insurmountable  $E_{\text{act}}$  of 2.93 eV, which means that the stage of  $^*\text{O}_2 \rightarrow ^*\text{O} + ^*\text{O}$  on  $\text{Co-N}_4\text{-C}_{64}$  is extremely thermodynamically and kinetically disadvantageous. The

dissociation details are illustrated in Fig. 7a. Conversely, the hydrogenation of  $^*\text{O}_2$  to  $^*\text{OOH}$  is more feasible because for  $^*\text{O}_2 + ^*\text{H} \rightarrow ^*\text{OOH}$ , this reaction has an exothermic reaction energy of 0.69 eV. Moreover, this process is accompanied by a very low  $E_{\text{act}}$  of 0.13 eV, which is evidently lower than the  $E_{\text{ads}}$  of  $^*\text{O}_2$  (−0.57 eV) on  $\text{Co-N}_4\text{-C}_{64}$ . The  $V_{\text{freq}}$  of TS8 is  $i981\text{ cm}^{-1}$ . The hydrogenation details (see Fig. 7b) indicate that  $d_{\text{O-H}}$  decreases from 1.993 Å in IS8 to 1.356 Å in TS8 and to 0.982 Å in FS8. Meanwhile,  $d_{\text{Co-O}}$  shortens from 1.859 Å in IS8 to 1.838 Å in FS8, and  $d_{\text{O-O}}$  increases from 1.295 Å in IS8 to 1.416 Å in FS8. This implies that the interaction between Co–O is strengthened and that between O–O is weakened.

For the formed  $^*\text{OOH}$ , there are two conceivable hydrogenation pathways: the  $^*\text{H}$  attacks the O atom that bonds to Co to afford  $^*\text{H}_2\text{O}_2$  ( $^*\text{OOH} + ^*\text{H} \rightarrow ^*\text{H}_2\text{O}_2$ ), or  $^*\text{H}$  attacks the hydroxyl oxygen in  $^*\text{OOH}$  to afford  $^*\text{O}$  and  $^*\text{H}_2\text{O}$  ( $^*\text{OOH} + ^*\text{H} \rightarrow ^*\text{O} + ^*\text{H}_2\text{O}$ ).

For  $^*\text{OOH} + ^*\text{H} \rightarrow \text{H}_2\text{O}_2$ , this reaction has an exothermic reaction energy of 0.46 eV. Moreover, this process is accompanied by an  $E_{\text{act}}$  of 0.80 eV, which is obviously lower than the  $E_{\text{ads}}$  of  $^*\text{OOH}$  (−1.54 eV) on  $\text{Co-N}_4\text{-C}_{64}$ . The hydrogenation details

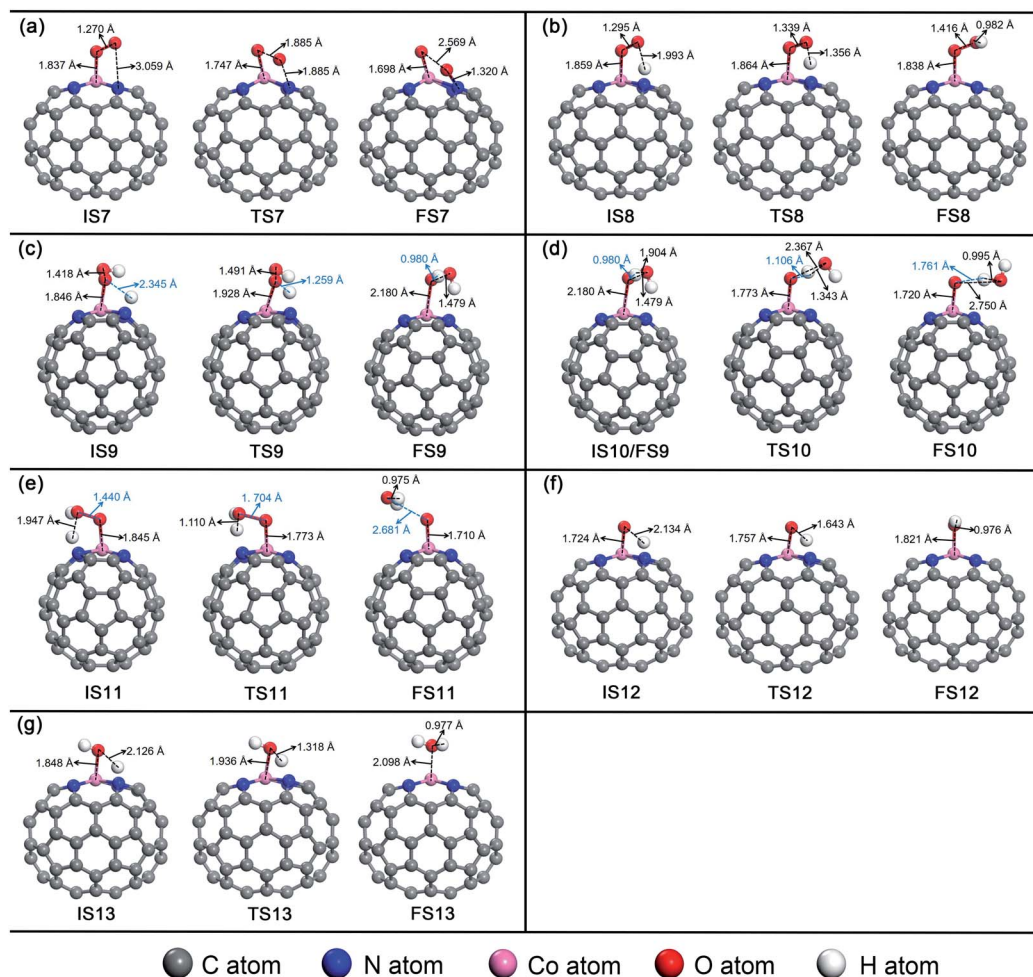


Fig. 7 The detailed process of the ORR on  $\text{Co-N}_4\text{-C}_{64}$ . (a)  $^*\text{O}_2 \rightarrow ^*\text{O} + ^*\text{O}$ , (b)  $^*\text{O}_2 + ^*\text{H} \rightarrow ^*\text{OOH}$ , (c)  $^*\text{OOH} + ^*\text{H} \rightarrow ^*\text{H}_2\text{O}_2$ , (d)  $^*\text{H}_2\text{O}_2 \rightarrow ^*\text{O} + ^*\text{H}_2\text{O}$ , (e)  $^*\text{OOH} + ^*\text{H} \rightarrow ^*\text{O} + ^*\text{H}_2\text{O}$ , (f)  $^*\text{O} + ^*\text{H} \rightarrow ^*\text{OH}$ , and (g)  $^*\text{OH} + ^*\text{H} \rightarrow ^*\text{H}_2\text{O}$ .



(see Fig. 7c) indicate that  $^*\text{H}$  attacks the O atom that bonds to Co, and  $d_{\text{O-H}}$  decreases from 2.345 Å in IS9 to 0.980 Å in FS9. Moreover,  $d_{\text{Co-O}}$  increases from 1.846 Å in IS9 to 2.180 Å in FS9. The generated  $\text{H}_2\text{O}_2$  is adsorbed on  $\text{Co-N}_4\text{-C}_{64}$  with an  $E_{\text{ads}}$  of  $-0.70$  eV. Then,  $^*\text{H}_2\text{O}_2$  is instantly decomposed to  $^*\text{O} + ^*\text{H}_2\text{O}$  because the reaction of  $^*\text{H}_2\text{O}_2 \rightarrow ^*\text{O} + ^*\text{H}_2\text{O}$  has an exothermic energy of 0.23 eV with a very low  $E_{\text{act}}$  of 0.33 eV, which means that the stage of  $^*\text{H}_2\text{O}_2 \rightarrow ^*\text{O} + ^*\text{H}_2\text{O}$  on  $\text{Co-N}_4\text{-C}_{64}$  is advantageous both thermodynamically and kinetically. Moreover, the energy required for this stage is lower than the  $E_{\text{ads}}$  of  $^*\text{H}_2\text{O}_2$  ( $-0.70$  eV) on  $\text{Co-N}_4\text{-C}_{64}$ . It can be seen that although the  $^*\text{H}_2\text{O}_2$  on  $\text{Co-N}_4\text{-C}_{64}$  is formed by the  $2e^-$  path, both thermodynamics and kinetics character enable its decomposition reaction to pass through the favorable  $4e^-$  path again. The decomposition details (see Fig. 7d) indicate that the  $^*\text{H}$  on the O atom that bonds to Co is transferred to the adjacent hydroxyl oxygen to generate the first  $^*\text{H}_2\text{O}$ , and the generated  $^*\text{H}_2\text{O}$  can be effortlessly separated from the  $\text{Co-N}_4\text{-C}_{64}$  surface, which only requires 0.43 eV. Meanwhile,  $d_{\text{Co-O}}$  shortens from 2.180 Å in IS10/FS9 to 1.720 Å in FS10 and  $d_{\text{O-O}}$  increases from 1.479 Å in IS10 to 2.750 Å in FS10, which implies that the interaction between Co-O is strengthened and the O-O bond is broken. The  $V_{\text{freq}}$  of  $i1469\text{ cm}^{-1}$  for TS9 and  $i627\text{ cm}^{-1}$  for TS10 respectively describe the formation and the decomposition of  $^*\text{H}_2\text{O}_2$ .

For  $^*\text{OOH} + ^*\text{H} \rightarrow ^*\text{O} + ^*\text{H}_2\text{O}$ , this reaction has an exothermic reaction energy of 0.41 eV. Moreover, this process is accompanied by an  $E_{\text{act}}$  of 0.78 eV, which is obviously lower than the  $E_{\text{ads}}$  of  $^*\text{OOH}$  ( $-1.54$  eV) on  $\text{Co-N}_4\text{-C}_{64}$ . The  $V_{\text{freq}}$  of  $i768\text{ cm}^{-1}$  in TS11 exactly exhibits the formation of  $^*\text{H}_2\text{O}$ , and the formed  $^*\text{H}_2\text{O}$  can easily detach from the  $\text{Co-N}_4\text{-C}_{64}$  surface, which only requires 0.26 eV. The hydrogenation details (see Fig. 7e) indicate that  $d_{\text{Co-O}}$  shortens from 1.845 Å in IS11 to 1.710 Å in FS11 and that  $d_{\text{O-O}}$  increases from 1.440 Å in IS11 to 2.681 Å in FS11; these findings respectively indicate that the interaction between Co-O is strengthened and the O-O bond is broken.

The above results manifest that for  $^*\text{OOH}$ , regardless of whether it is first hydrogenated to form  $^*\text{H}_2\text{O}_2$  and then decomposed to  $^*\text{O} + ^*\text{H}_2\text{O}$  or whether  $^*\text{OOH}$  is directly hydrogenated to  $^*\text{O} + ^*\text{H}_2\text{O}$ , it is conducive to ORR behavior on  $\text{Co-N}_4\text{-C}_{64}$ .

After the  $^*\text{H}_2\text{O}$  is released, the atomic O remaining on Co experiences continuous hydrogenation to afford the second  $^*\text{H}_2\text{O}$ :  $^*\text{O} + ^*\text{H} \rightarrow ^*\text{OH}$  and  $^*\text{OH} + ^*\text{H} \rightarrow ^*\text{H}_2\text{O}$ . The former reaction has a whopping exothermic reaction energy of 2.10 eV. Moreover, this process is accompanied by a very low  $E_{\text{act}}$  of 0.04 eV, which is significantly lower than the  $E_{\text{ads}}$  of  $^*\text{O}$  ( $-2.62$  eV) on  $\text{Co-N}_4\text{-C}_{64}$ . The hydrogenation details (see Fig. 7f) indicate that  $d_{\text{O-H}}$  diminishes from 2.134 Å in IS12 to 0.976 Å in FS12.  $d_{\text{Co-O}}$  lengthens from 1.724 Å in IS12 to 1.821 Å in FS12, which manifests that the interaction between Co-O is weakened with the formation of  $^*\text{OH}$ . Then, the  $^*\text{OH}$  remaining on Co experiences the succeeding hydrogenation:  $^*\text{OH} + ^*\text{H} \rightarrow ^*\text{H}_2\text{O}$ . This stage has an exothermic reaction energy of 0.86 eV. Moreover, this process is accompanied by a very low  $E_{\text{act}}$  of 0.22 eV, which is evidently lower than the  $E_{\text{ads}}$  of  $^*\text{OH}$  ( $-2.54$  eV) on  $\text{Co-N}_4\text{-C}_{64}$ . The hydrogenation details (see Fig. 7g) indicate

that  $d_{\text{Co-O}}$  lengthens from 1.848 Å in IS13 to 2.098 Å in FS13; this indicates that the interaction between Co-O is weakened and the formed  $^*\text{H}_2\text{O}$  can be effortlessly detached from the  $\text{Co-N}_4\text{-C}_{64}$  surface due to the low  $E_{\text{ads}}$  of  $-0.60$  eV. The  $V_{\text{freq}}$  values of  $i918\text{ cm}^{-1}$  for TS12 and  $i1467\text{ cm}^{-1}$  for TS13 respectively describe the formation of  $^*\text{OH}$  and the second  $^*\text{H}_2\text{O}$ .

**3.4.3 ORR mechanisms on  $\text{Ni-N}_4\text{-C}_{64}$ .** The ORR mechanisms on  $\text{Ni-N}_4\text{-C}_{64}$  are also discussed. Firstly, the positive  $E_{\text{ads}}$  of 0.33 eV for  $^*\text{O}_2$  on  $\text{Ni-N}_4\text{-C}_{64}$  demonstrates that the ORR activity of  $\text{Ni-N}_4\text{-C}_{64}$  is unsatisfactory. Fig. 8 shows the  $4e^-$  pathway through which the  $^*\text{O}_2$  on the  $\text{Ni-N}_4\text{-C}_{64}$  is hydrogenated to  $^*\text{OOH}$ , then to  $^*\text{O} + ^*\text{H}_2\text{O}$ ; finally, the atomic O remaining on Ni is continuously hydrogenated. As can be viewed in Fig. 8, the stage of  $^*\text{OOH} + ^*\text{H} \rightarrow ^*\text{O} + ^*\text{H}_2\text{O}$  requires an endothermic reaction energy of 0.21 eV to complete. Moreover, the two stages for  $^*\text{O} + ^*\text{H} \rightarrow ^*\text{OH}$  and  $^*\text{OH} + ^*\text{H} \rightarrow ^*\text{H}_2\text{O}$  have extremely high energy barriers (3.25 eV and 2.97 eV). In conclusion,  $\text{Ni-N}_4\text{-C}_{64}$  is unfavorable as an ORR electrocatalyst.

### 3.5 PES and relative energy

The relative energy curve can be utilised as an effective method to assess the ORR properties of  $\text{M-N}_4\text{-C}_{64}$  ( $\text{M} = \text{Fe}, \text{Co}, \text{and Ni}$ ). Fig. 9a-c exhibit the potential energy surface (PES) diagrams of  $\text{Fe-N}_4\text{-C}_{64}$ ,  $\text{Co-N}_4\text{-C}_{64}$ , and  $\text{Ni-N}_4\text{-C}_{64}$ , correspondingly. In Fig. 9a and b, the green line denotes the stage of  $^*\text{O}_2 \rightarrow ^*\text{O} + ^*\text{O}$ . The blue line in Fig. 9a denotes the stage of  $^*\text{OOH} + ^*\text{H} \rightarrow$

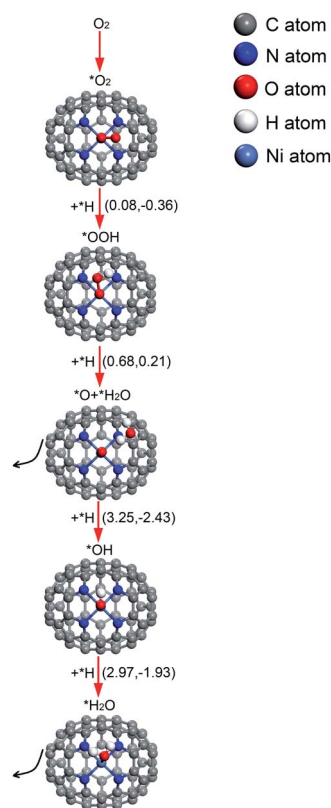


Fig. 8 The conceivable ORR pathway on  $\text{Ni-N}_4\text{-C}_{64}$ . The value on the left in parentheses is the activation energy and the value on the right is the reaction energy (in eV). \* indicates adsorbed species.



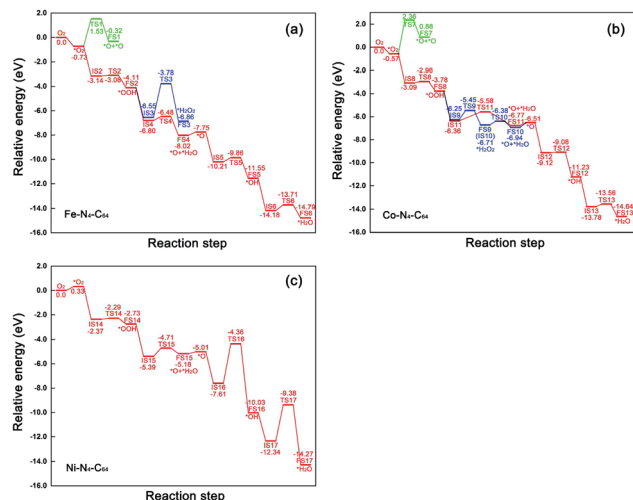


Fig. 9 Relative energy profiles of the conceivable ORR pathways on (a) Fe-N<sub>4</sub>-C<sub>64</sub>, (b) Co-N<sub>4</sub>-C<sub>64</sub> and (c) Ni-N<sub>4</sub>-C<sub>64</sub>.

\*H<sub>2</sub>O<sub>2</sub> on Fe-N<sub>4</sub>-C<sub>64</sub>, and that in Fig. 9b denotes the two stages of \*OOH + \*H → \*H<sub>2</sub>O<sub>2</sub> and \*H<sub>2</sub>O<sub>2</sub> → \*O + \*H<sub>2</sub>O on Co-N<sub>4</sub>-C<sub>64</sub>. For the red line path that can promote ORR on Fe-N<sub>4</sub>-C<sub>64</sub> (see Fig. 9a), the first stage is to hydrogenate \*O<sub>2</sub> to \*OOH; \*OOH is then hydrogenated to \*O + \*H<sub>2</sub>O, and finally the atomic O remaining on Fe is continuously hydrogenated. The rate-limiting step (RLS) for the favorable red line path on Fe-N<sub>4</sub>-C<sub>64</sub> is \*OH + \*H → \*H<sub>2</sub>O with an  $E_{\text{act}}$  of 0.47 eV. Moreover, the entire reaction energy variation of the red line path on Fe-N<sub>4</sub>-C<sub>64</sub> is degressive, which is conducive to positive-going reactions. Co-N<sub>4</sub>-C<sub>64</sub> can facilitate the ORR *via* two different paths (see Fig. 9b). One of the two paths is consistent with the aforementioned favorable ORR red line path on Fe-N<sub>4</sub>-C<sub>64</sub>. The RLS for this advantageous red line path on Co-N<sub>4</sub>-C<sub>64</sub> is \*OOH + \*H → \*O + \*H<sub>2</sub>O with an  $E_{\text{act}}$  of 0.78 eV. For the other path, the difference from the red line path is that the intermediate \*OOH in this path is hydrogenated to \*H<sub>2</sub>O<sub>2</sub>. The generated \*H<sub>2</sub>O<sub>2</sub> is immediately decomposed into \*O + \*H<sub>2</sub>O to continue the 4e<sup>−</sup> path because this stage has an exothermic reaction energy of 0.23 eV with a much lower  $E_{\text{act}}$  (0.33 eV) than the  $E_{\text{ads}}$  of \*H<sub>2</sub>O<sub>2</sub> (−0.70 eV); finally, the atomic O remaining on Co is continuously hydrogenated. Moreover, the RLS for this feasible path on Co-N<sub>4</sub>-C<sub>64</sub> is \*OOH + \*H → \*H<sub>2</sub>O<sub>2</sub> with an  $E_{\text{act}}$  of 0.80 eV. The entire reaction energy variation of the two favorable ORR paths on Co-N<sub>4</sub>-C<sub>64</sub> is degressive, which is conducive to positive-going reactions. Meanwhile, Fig. 9c intuitively shows that Ni-N<sub>4</sub>-C<sub>64</sub> as an ORR electrocatalyst is an unfavorable choice because the two stages for \*O + \*H → \*OH and \*OH + \*H → \*H<sub>2</sub>O possess high energy barriers.

## 4. Conclusions

In this work, the density functional method was utilized to systematically study the co-doping of transition metal M and heteroatom N<sub>4</sub> in vacancy fullerene (M-N<sub>4</sub>-C<sub>64</sub>, M = Fe, Co, and Ni) as a novel type of non-precious ORR electrocatalyst. The

calculated formation energies indicated that Fe-N<sub>4</sub>-C<sub>64</sub>, Co-N<sub>4</sub>-C<sub>64</sub> and Ni-N<sub>4</sub>-C<sub>64</sub> are thermodynamically stable. Mulliken charge studies manifested that the metal center is the reaction site of the ORR and that the electron transfer from the metal center to N<sub>4</sub>-C<sub>64</sub> is the largest in the Fe-N<sub>4</sub>-C<sub>64</sub> system. PDOS revealed that the interaction between Fe-N<sub>4</sub>-C<sub>64</sub> and the adsorbate is the strongest among the three, followed by Co-N<sub>4</sub>-C<sub>64</sub> and finally Ni-N<sub>4</sub>-C<sub>64</sub>. The results of the calculated adsorption energies are consistent with the PDOS analysis. By analyzing and comparing the adsorption energies of the ORR species and the activation energies and reaction energies of all the basic ORR reaction steps involved in M-N<sub>4</sub>-C<sub>64</sub>, two favorable ORR electrocatalysts, Fe-N<sub>4</sub>-C<sub>64</sub> and Co-N<sub>4</sub>-C<sub>64</sub>, were selected. Meanwhile, favorable ORR paths on Fe-N<sub>4</sub>-C<sub>64</sub> and Co-N<sub>4</sub>-C<sub>64</sub> were determined, and both catalysts used 4e<sup>−</sup> mechanisms to facilitate ORR. For Fe-N<sub>4</sub>-C<sub>64</sub>, the intermediate \*OOH formed by hydrogenation of \*O<sub>2</sub> on Fe-N<sub>4</sub>-C<sub>64</sub> continues to be hydrogenated to \*O + \*H<sub>2</sub>O, and finally, the \*O remaining on Fe is continuously hydrogenated. The rate-limiting step (RLS) for the favorable path on Fe-N<sub>4</sub>-C<sub>64</sub> is \*OH + \*H → \*H<sub>2</sub>O, with an  $E_{\text{act}}$  of 0.47 eV. For Co-N<sub>4</sub>-C<sub>64</sub>, the intermediate \*OOH formed by hydrogenation of \*O<sub>2</sub> on Co-N<sub>4</sub>-C<sub>64</sub> can be directly hydrogenated to \*O + \*H<sub>2</sub>O or firstly hydrogenated to \*H<sub>2</sub>O<sub>2</sub> and then promptly decomposes to \*O + \*H<sub>2</sub>O; finally, the \*O remaining on Co is continuously hydrogenated. The RLS of the two advantageous paths on Co-N<sub>4</sub>-C<sub>64</sub> is the hydrogenation stage of the intermediate \*OOH, and the corresponding activation energies are 0.78 eV for \*OOH + \*H → \*O + \*H<sub>2</sub>O and 0.80 eV for \*OOH + \*H → \*H<sub>2</sub>O<sub>2</sub>, correspondingly. PES diagrams intuitively reflect that the whole reaction energy variation in the favorable ORR paths of Fe-N<sub>4</sub>-C<sub>64</sub> and Co-N<sub>4</sub>-C<sub>64</sub> is degressive, which is conducive to positive-going reactions. This study demonstrates that Fe-N<sub>4</sub>-C<sub>64</sub> and Co-N<sub>4</sub>-C<sub>64</sub> are high-efficiency ORR electrocatalysts. We expect that the proposed transition metal and heteroatom N<sub>4</sub> co-doped in vacancy fullerene can contribute to the development of cathode materials for FCs.

## Conflicts of interest

There are no conflicts to declare.

## Acknowledgements

This work is supported by the National Natural Science Foundation of China (No. 21573090), and Scientific Research Fund of Jilin Provincial Education Department (2015437) for financial support of this research.

## References

- 1 Y. Wang, K. S. Chen, J. Mishler, S. C. Cho and X. C. Adroher, *Appl. Energy*, 2011, **88**, 981–1007.
- 2 S. Sui, X. Wang, X. Zhou, Y. Su, S. B. Riffat and C. Liu, *J. Mater. Chem.*, 2017, **5**, 1808–1825.
- 3 S. Wang and S. P. Jiang, *Natl. Sci. Rev.*, 2017, **4**, 163–166.





- 4 E. H. Majlan, D. Rohendi, W. R. W. Daud, T. Husaini and M. A. Haque, *Renew. Sust. Energ. Rev.*, 2018, **89**, 117–134.
- 5 K. Gong, F. Du, Z. Xia, M. F. Durstock and L. Dai, *Science*, 2009, **323**, 760–764.
- 6 Y. Jiao, Y. Zheng, M. Jaroniec and S. Qiao, *Chem. Soc. Rev.*, 2015, **44**, 2060–2086.
- 7 C. Zhu, H. Li, S. Fu, D. Du and Y. Lin, *Chem. Soc. Rev.*, 2016, **45**, 517–531.
- 8 C. Zhu, S. Fu, Q. Shi, D. Du and Y. Lin, *Angew. Chem., Int. Ed.*, 2017, **56**, 13944–13960.
- 9 H. A. Gasteiger, S. S. Kocha, B. Sompalli and F. T. Wagner, *Appl. Catal. B-Environ.*, 2005, **56**, 9–35.
- 10 Y. Zheng, D. Yang, J. M. Kweun, C. Li, K. Tan, F. Kong, C. Liang, Y. J. Chabal, Y. Y. Kim and M. Cho, *Nano Energy*, 2016, **30**, 443–449.
- 11 Z. Liang, H. Zheng and R. Cao, *Sustain. Energy Fuels*, 2020, **4**, 3848–3870.
- 12 M. K. Debe, *Nature*, 2012, **486**, 43–51.
- 13 J. Liu, M. Jiao, B. Mei, Y. Tong, Y. Li, M. Ruan, P. Song, G. Sun, L. Jiang and Y. Wang, *Angew. Chem., Int. Ed.*, 2019, **58**, 1163–1167.
- 14 L. Liu, G. Zeng, J. Chen, L. Bi, L. Dai and Z. Wen, *Nano Energy*, 2018, **49**, 393–402.
- 15 X. Ren, Q. Lv, L. Liu, B. Liu, Y. Wang, A. Liu and G. Wu, *Sustain. Energy Fuels*, 2020, **4**, 15–30.
- 16 J. Kim, H. Kim and H. Lee, *Chemsuschem*, 2018, **11**, 104–113.
- 17 B. Lu, Q. Liu and S. Chen, *ACS Catal.*, 2020, **10**, 7584–7618.
- 18 H. Fei, J. Dong, M. J. Arellanojimenez, G. Ye, N. D. Kim, E. L. G. Samuel, Z. Peng, Z. Zhu, F. Qin and J. Bao, *Nat. Commun.*, 2015, **6**, 8668.
- 19 H. J. Qiu, Y. Ito, W. Cong, Y. Tan, P. Liu, A. Hirata, T. Fujita, Z. Tang and M. Chen, *Angew. Chem., Int. Ed.*, 2015, **54**, 14031–14035.
- 20 C. Zhao, X. Dai, T. Yao, W. Chen, X. Wang, J. Wang, J. Yang, S. Wei, Y. Wu and Y. Li, *J. Am. Chem. Soc.*, 2017, **139**, 8078–8081.
- 21 X. Wang, Z. Chen, X. Zhao, T. Yao, W. Chen, R. You, C. Zhao, G. Wu, J. Wang and W. Huang, *Angew. Chem., Int. Ed.*, 2018, **57**, 1944–1948.
- 22 P. Chen, T. Zhou, L. Xing, K. Xu, Y. Tong, H. Xie, L. Zhang, W. Yan, W. Chu and C. Wu, *Angew. Chem., Int. Ed.*, 2017, **56**, 610–614.
- 23 M. Xiao, J. Zhu, L. Ma, Z. Jin, J. Ge, X. Deng, Y. Hou, Q. He, J. Li, Q. Jia, S. Mukerjee, R. Yang, Z. Jiang, D. Su, C. Liu and W. Xing, *ACS Catal.*, 2018, **8**, 2824–2832.
- 24 X. Yang, A. Wang, B. Qiao, J. Li, J. Liu and T. Zhang, *Acc. Chem. Res.*, 2013, **46**, 1740–1748.
- 25 T. Xu, W. Shen, W. Huang and X. Lu, *Mater. Today Nano*, 2020, **11**, 100081.
- 26 K. Minami, Y. Kasuya, T. Yamazaki, Q. Ji, W. Nakanishi, J. P. Hill, H. Sakai and K. Ariga, *Adv. Mater.*, 2015, **27**, 4020–4026.
- 27 Z. Tan, K. Ni, G. Chen, W. Zeng, Z. Tao, M. Ikram, Q. Zhang, H. Wang, L. Sun and X. Zhu, *Adv. Mater.*, 2017, **29**, 1603414.
- 28 L. Rincongarcia, A. K. Ismael, C. Evangeli, I. Grace, G. Rubiobollinger, K. Porfyraakis, N. Agrait and C. J. Lambert, *Nat. Mater.*, 2016, **15**, 289–293.
- 29 K. Liu, S. Gao, Z. Zheng, X. Deng, S. Mukherjee, S. Wang, H. Xu, J. Wang, J. Liu, T. Zhai and Y. Fang, *Adv. Mater.*, 2019, **31**, e1808254.
- 30 J. M. Hawkins, A. Meyer and M. A. Solow, *J. Am. Chem. Soc.*, 1993, **115**, 7499–7500.
- 31 K. Choho, W. Langenaeker, G. V. De Woude and P. Geerlings, *J. Mol. Struct.*, 1995, **338**, 293–301.
- 32 M. R. Benzigar, S. Joseph, H. Ilbeygi, D. Park, S. Sarkar, G. K. Chandra, S. Umapathy, S. Srinivasan, S. N. Talapaneni and A. Vinu, *Angew. Chem., Int. Ed.*, 2018, **57**, 569–573.
- 33 M. R. Benzigar, S. Joseph, A. V. Baskar, D. Park, G. K. Chandra, S. Umapathy, S. N. Talapaneni and A. Vinu, *Adv. Funct. Mater.*, 2018, **28**, 1803701.
- 34 Y. Lin and D. S. Su, *ACS Nano*, 2014, **8**, 7823–7833.
- 35 S. Gao, X. Wei, H. Fan, L. Li, K. Geng and J. Wang, *Nano Energy*, 2015, **13**, 518–526.
- 36 X. Chen, J. Chang and Q. Ke, *Carbon*, 2018, **126**, 53–57.
- 37 Y. Wang, M. Jiao, W. Song and Z. Wu, *Carbon*, 2017, **114**, 393–401.
- 38 F. Banhart, J. Kotakoski and A. V. Krashenninnikov, *ACS Nano*, 2011, **5**, 26–41.
- 39 Y. Chen, S. Ji, C. Chen, Q. Peng, D. Wang and Y. Li, *Joule*, 2018, **2**, 1242–1264.
- 40 D. H. Lee, W. J. Lee, W. J. Lee, S. O. Kim and Y.-H. Kim, *Phys. Rev. Lett.*, 2011, **106**, 175502.
- 41 H. Fei, J. Dong, Y. Feng, C. S. Allen, C. Wan, B. Voloskiy, M. Li, Z. Zhao, Y. Wang, H. Sun, P. An, W. Chen, Z. Guo, C. Lee, D. Chen, I. Shakir, M. Liu, T. Hu, Y. Li, A. I. Kirkland, X. Duan and Y. Huang, *Nat. Catal.*, 2018, **1**, 63–72.
- 42 Y. Chen, S. Ji, Y. Wang, J. Dong, W. Chen, Z. Li, R. Shen, L. Zheng, Z. Zhuang and D. Wang, *Angew. Chem., Int. Ed.*, 2017, **56**, 6937–6941.
- 43 X. Li, S. Xi, L. Sun, S. Dou, Z. Huang, T. Su and X. Wang, *Adv. Sci.*, 2020, **7**, 2001545.
- 44 F. Callevallejo, J. I. Martinez and J. Rossmeisl, *Phys. Chem. Chem. Phys.*, 2011, **13**, 15639–15643.
- 45 S. Kattel and G. Wang, *J. Mater. Chem.*, 2013, **1**, 10790–10797.
- 46 S. Kattel and G. Wang, *J. Phys. Chem. Lett.*, 2014, **5**, 452–456.
- 47 X. Chen, R. Hu and F. Bai, *Materials*, 2017, **10**, 549.
- 48 B. Modak, K. Srinivasu and S. K. Ghosh, *Int. J. Hydrogen Energy*, 2017, **42**, 2278–2287.
- 49 B. Delley, *J. Chem. Phys.*, 2000, **113**, 7756–7764.
- 50 J. P. Perdew, K. Burke and M. Ernzerhof, *Phys. Rev. Lett.*, 1996, **77**, 3865–3868.
- 51 K. Liu, S. Kattel, V. Mao and G. Wang, *J. Phys. Chem. C*, 2016, **120**, 1586–1596.

